Journal of Sound and Vibration 531 (2022) 116977

Contents lists available at ScienceDirect

Journal of Sound and Vibration

journal homepage: www.elsevier.com/locate/jsvi

Rapid Communications

Metadamping in inertially amplified metamaterials: Trade-off between spatial attenuation and temporal attenuation

Mahmoud I. Hussein [a,b,*], Ibrahim Patrick [c], Arnab Banerjee [d], Sondipon Adhikari [e]

[a] Ann and HJ Smead Department of Aerospace Engineering Sciences, University of Colorado Boulder, Boulder, Colorado 80303, USA
[b] Department of Physics, University of Colorado Boulder, Boulder, Colorado 80302, USA
[c] Faculty of Science and Engineering, Swansea University, Swansea, UK
[d] Department of Civil Engineering, Indian Institute of Technology, Delhi, India
[e] James Watt School of Engineering, The University of Glasgow, Glasgow, UK

ARTICLE INFO

Keywords:
Metadamping
Inertial amplification
Local resonance
Temporal attenuation
Spatial attenuation
Elastic metamaterial
Phononics

ABSTRACT

Metadamping is the phenomenon of either enhanced or diminished intrinsic dissipation in a material stemming from the material's internal structural dynamics. It has previously been shown that a locally resonant elastic metamaterial may be designed to exhibit higher or lower dissipation compared to a statically equivalent phononic crystal with the same amount of prescribed damping. Here we reveal that even further dissipation, or alternatively further reduction of loss, may be reached in an inertially amplified metamaterial that is also statically equivalent and has the same amount of prescribed damping. This is demonstrated by a passive configuration whereby an attenuation peak is generated by the motion of a mass supported by an inclined lever arm. We further show that by coupling this inertially amplified attenuation peak with that of a local-resonance attenuation peak, a trade-off between the intensity of spatial attenuation versus temporal attenuation is realized for a range of the inclination angle. Design for performance along this trade-off is therefore possible by adjustment of the lever angle. A regime of monotonic increase in both attenuation types is also possible for a different range of the inclination angle. These findings open the way for highly expanding the Ashby space for stiffness-damping capacity or stiffness-spatial attenuation capacity through design of the internal structure of materials.

1. Introduction

Control of dissipation is one of the key design factors in structural dynamics. Dissipation is a measure of loss of energy as a function of time. In a finite structure, the dissipation characteristics have a spatial and frequency dependency. In an infinite medium, such as a waveguide or a structured material, dissipation exhibits also a wavenumber (or wavevector) dependency [1–4]. Representation of dissipation as an intrinsic wavenumber-dependent quantity provides a fundamental measure that is independent of global dimensions, boundary conditions, and nature of forcing. This measure is obtained by considering a representative unit cell of the medium of interest, applying Bloch's theorem on the unit cell, and calculating the wavenumber-dependent damping ratio alongside the wavenumber-dependent damped frequency. Upon integration of each damping ratio branch over the Brillouin zone (BZ), and possibly summing over all branches, a total cumulative measure of dissipation is obtained–which provides a measure of the overall damping

* Corresponding author.
E-mail address: mih@colorado.edu (M.I. Hussein).

https://doi.org/10.1016/j.jsv.2022.116977
Received 15 November 2021; Received in revised form 16 April 2022; Accepted 21 April 2022
Available online 23 April 2022

capacity of the medium or material under consideration [5].

Phononic materials, such as phononic crystals and elastic metamaterials, provide an opportunity for unit cell design not only to generate band gaps for spatial attenuation but also to control the level of dissipation [6–8]. In phononic crystals, the band structure is shaped by interferences of transmitted and reflected waves from periodic inclusions, interfaces, and/or boundaries within the medium [9–11]. In an elastic metamaterial, which is often also periodic, the band structure is shaped not only by wave interferences but also by couplings–or hybridizations–between substructure-resonance modes and elastic-wave modes in the hosting medium [12,13]. Upon comparing the dissipation across the BZ for an elastic metamaterial and a statically equivalent phononic crystal with the same level of prescribed damping, it was shown that the former may be designed to enable enhanced dissipation, a concept termed *metadamping* [5, 14]. In some cases, the elastic-metamaterial unit cell may be designed to exhibit diminished dissipation, which is negative metadamping [15–18]. Since its inception in 2013 [5], metadamping has been explored in a variety of configurations, including ones featuring negative stiffness [19] and non-local resonance [17], and, recently, in materials with electrically activated local resonances [20,21].

In this work, we investigate metadamping in inertially amplified (IA) metamaterials [22–25]. Inertial amplification (IA) contrasts with local resonance in that it involves a mechanical mechanism to provide a magnification of the “effective inertia" of the massive portions or components of the system. Unlike local resonance, an IA metamaterial will exhibit a band gap due to inertial coupling. This concept may be realized using a lever-arm effect that allows the inertia of a given mass to be magnified to a degree proportional to the arm length. We show that an IA metamaterial may be passively tuned to exhibit a significant further boost in the damping capacity (positive metadamping) or in the reduction of loss (negative metadamping), compared to the improvements attained by a statically equivalent locally resonant elastic metamaterial. We examine this behavior in a 1D chain model that encompasses both an IA mass and a local-resonance mass separately attached to the baseline mass [26]. This configuration yields a two degrees-of-freedom system with a bounded band gap that features two coupled resonances. In addition to the extreme metadamping behavior, this configuration reveals a novel regime whereby a trade-off between the intensities of temporal attenuation (dissipation) and spatial attenuation (band-gap behavior) takes effect. These findings have potentially far-reaching implications on the design of future phononic materials with tailored space-time attenuation characteristics.

2. Inertially amplified chain: configuration and mathematical model

We consider a one-dimensional infinite chain where the unit cell consists of a base mass M connected to the adjacent mass by a spring with stiffness K_{IA} and a viscous damping dashpot with damping constant C, where the spring and damper act in parallel. Each baseline mass is also connected to its neighbor by an inertial-amplifier attachment which comprises an auxiliary mass m_a, referred to as the mass of the inertial amplifier, and a rigid link; thus, the inertial amplifier itself is connected to a pair of baseline masses by rigid links. This inertial-amplifier mass plays the key role of inducing inertial amplification, as its acceleration is amplified owing to the lever-based connecting mechanism. Furthermore, in our most general configuration, a single-degree-of-freedom linear mass resonator, comprising a spring and viscous damping dashpot placed in parallel, is attached to the baseline mass in the unit cell. The mass, spring, and damping constants of the resonator are m, k, and c, respectively. The resonator’s modal degree of freedom couples with the modal degree of freedom associated with the inertially amplified mass and creates a band gap with a double-attenuation peak in the imaginary part of the complex dispersion diagram; this aspect is discussed and analyzed in the next sections. The equation of motion of the resonating mass is

$$m\ddot{w}_n + c(\dot{w}_n - \dot{u}_n) + k_{1A}(w_n - u_n) = 0, \tag{1}$$

where u_n and w_n denote the displacement of the baseline mass and the resonator mass, respectively, and the number of overhead dots indicates the order of derivative with respect to time.

2.1. Force on the baseline mass from the inertial-amplifier mass

For the n^{th} unit cell, the kinematic relationship between the acceleration of the auxiliary mass $\ddot{v}_n$ and the acceleration of the main mass $\ddot{u}_n$ and its preceding mass $\ddot{u}_{n-1}$ is expressed as

$$\ddot{v}_n = \frac{\left(\ddot{u}_n - \ddot{u}_{n-1}\right)}{2}\cot\alpha, \tag{2}$$

where α is the angle between the central axis of the IA chain and the rigid links of the inertial-amplifier attachment. If F_n is the force in the rigid links due to the net movement of the baseline masses in the n^{th} and $(n\text{-}1)^{\text{th}}$ unit cells, then the net force on the rigid links is calculated by balancing the forces on the inertial-amplifier mass in the following manner:

$$2F_n\sin\alpha = m_a\ddot{v}_n = \left(m_a\left(\ddot{u}_n - \ddot{u}_{n-1}\right)\right)\frac{\cot\alpha}{2}, \tag{3}$$

or

$$F_n = \frac{m_a\left(\ddot{u}_n - \ddot{u}_{n-1}\right)}{4(\sin\alpha)(\tan\alpha)}. \tag{4}$$

The component of the force, acting from the inertial-amplifier mass onto the baseline mass stemming from the net movement of the baseline masses in the n^{th} and $(n\text{-}1)^{\text{th}}$ unit cells, along the direction of the wave propagation is

$$\widetilde{F}_n = F_n\cos\alpha = \chi\left(m_a\left(\ddot{u}_n - \ddot{u}_{n-1}\right)\right), \tag{5}$$

where $\chi = 1/(4\tan^2\alpha)$. Similarly, we write

$$\widetilde{F}_{n+1} = F_{n+1}\cos\alpha = \chi\left(m_a\left(\ddot{u}_{n+1} - \ddot{u}_n\right)\right). \tag{6}$$

From Bloch's theorem,

$$u_{n+1} = u_n e^{i\mu} \text{ and } u_{n-1} = u_n e^{-i\mu}, \tag{7}$$

where $i = \sqrt{-1}$ is the imaginary number and μ is the wave-propagation constant, which can be written as $\mu = \kappa a$ where κ and a are the wavenumber and length of the lattice unit, respectively.

2.2. Equation of motion of the overall chain

The governing equation of motion for the n^{th} baseline mass of the overall inertial-amplifier chain is

$$M\ddot{u}_n + c(\dot{u}_n - \dot{w}_n) + k_{\text{IA}}(u_n - w_n) + C(2\dot{u}_n - \dot{u}_{n-1} - \dot{u}_{n+1}) + K_{\text{IA}}(2u_n - u_{n-1} - u_{n+1}) + \widetilde{F}_n - \widetilde{F}_{n+1} = 0. \tag{8}$$

Substituting Eqs. (5) and (6) into Eq. (8) produces

$$M\ddot{u}_n + c(\dot{u}_n - \dot{w}_n) + k_{\text{IA}}(u_n - w_n) + C(2\dot{u}_n - \dot{u}_{n-1} - \dot{u}_{n+1}) + K_{\text{IA}}(2u_n - u_{n-1} - u_{n+1}) + \chi\left(m_a\left(\ddot{u}_n - \ddot{u}_{n-1}\right)\right) - \chi\left(m_a\left(\ddot{u}_{n+1} - \ddot{u}_n\right)\right) = 0. \tag{9}$$

Substituting Eq. (7) in Eq. (9) yields

$$[M + 2\chi m_a(1-\cos\mu)]\ddot{u}_n + [c + 2C(1-cos\mu)]\dot{u}_n + [k_{\text{IA}} + 2K_{\text{IA}}(1-\cos\mu)]u_n - c\dot{w}_x - k_{\text{IA}}w_x = 0 \tag{10}$$

After substituting the definition of χ into Eq. (10), it can be written in matrix form as

$$\begin{bmatrix} M + \frac{1}{2}m_a(1-\cos\mu)\cot^2\alpha & 0 \\ 0 & m \end{bmatrix} + \begin{Bmatrix} \ddot{u}_n \\ \ddot{w}_x \end{Bmatrix} + \begin{bmatrix} c + 2C(1-\cos\mu) & -c \\ -c & c \end{bmatrix} \begin{Bmatrix} \dot{u}_n \\ \dot{w}_x \end{Bmatrix} + \begin{bmatrix} k_{\text{IA}} + 2K_{\text{IA}}(1-\cos\mu) & -k_{\text{IA}} \\ -k_{\text{IA}} & k_{\text{IA}} \end{bmatrix} \begin{Bmatrix} u_n \\ w_x \end{Bmatrix} = \begin{Bmatrix} 0 \\ 0 \end{Bmatrix}. \tag{11}$$

The reader may refer to Ref. [26] for an effective-dynamical properties analysis of a similar coupled IA-local resonance chain configuration.

To characterize the metadamping performance of the IA chain, we will also consider a statically equivalent phononic crystal (PnC) and a statically equivalent locally resonant acoustic metamaterial (AM). The governing equations for the PnC are

$$m_1\ddot{u}_n + (C+c)\dot{u}_n - c\dot{w}_n - C\dot{w}_{n-1} + (K_{\text{PnC}} + k_{\text{PnC}})u_n - k_{\text{PnC}}w_n - K_{\text{PnC}}w_{n-1} = 0, \tag{12}$$

$$m_2\ddot{w}_n + (C+c)\dot{w}_n - c\dot{u}_n - C\dot{u}_{n+1} + (K_{\text{PnC}} + k_{\text{PnC}})w_n - k_{\text{PnC}}u_n - K_{\text{PnC}}u_{n+1} = 0, \tag{13}$$

which, after implementing Bloch's theorem, can be written in matrix form as

$$\begin{bmatrix} m_1 & 0 \\ 0 & m_2 \end{bmatrix} \begin{Bmatrix} \ddot{u}_n \\ \ddot{w}_n \end{Bmatrix} + \begin{bmatrix} C+c & -c - Ce^{-i\kappa a} \\ -c - Ce^{i\kappa a} & C+c \end{bmatrix} \begin{Bmatrix} \dot{u}_n \\ \dot{w}_n \end{Bmatrix} + \begin{bmatrix} K_{\text{PnC}} + k_{\text{PnC}} & -k_{\text{PnC}} - K_{\text{PnC}}e^{-i\kappa a} \\ -k_{\text{PnC}} - K_{\text{PnC}}e^{i\kappa a} & K_{\text{PnC}} + k_{\text{PnC}} \end{bmatrix} \begin{Bmatrix} u_n \\ w_n \end{Bmatrix} = \begin{Bmatrix} 0 \\ 0 \end{Bmatrix}. \tag{14}$$

The governing equations for the AM are

$$m_1\ddot{u}_n + C(2\dot{u}_n - \dot{u}_{n-1} - \dot{u}_{n+1}) + c(\dot{u}_n - \dot{w}_n) + K_{\text{AM}}(2u_n - u_{n-1} - u_{n+1}) + k_{\text{AM}}(u_n - w_n) = 0, \tag{15}$$

$$m_2\ddot{w}_n + c(\dot{w}_n - \dot{u}_n) + k_{\text{AM}}(w_n - u_n) = 0, \tag{16}$$

which, after implementing Bloch's theorem, can be written in matrix form as

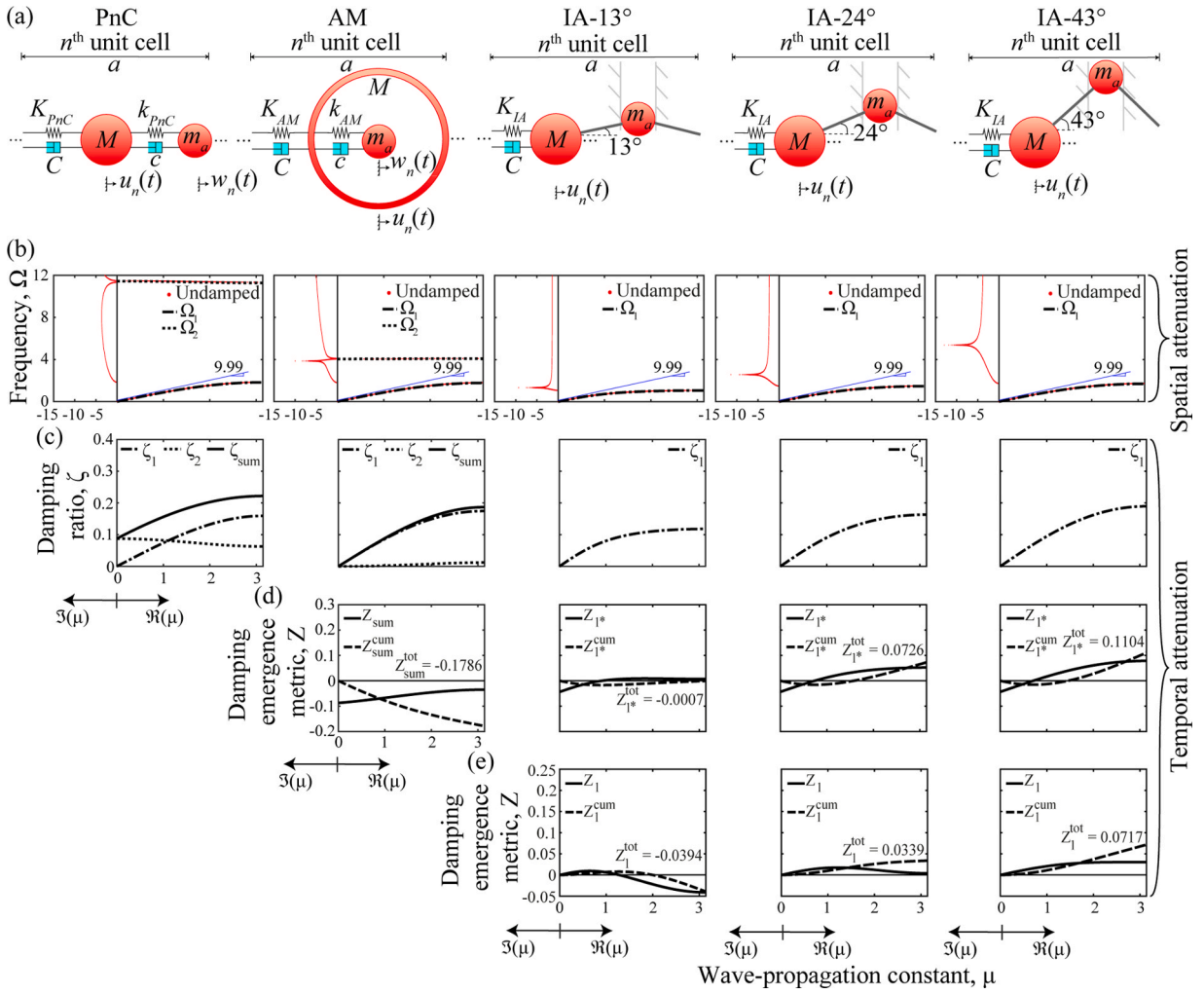

Fig. 1. Analysis of inertially amplified chain without a resonating mass. (a) Unit-cell schematics of statically equivalent chains, including a PnC, AM, and three variations of the IA chain exhibiting $\alpha = 13^{\circ}$, 24°, and 43°, respectively. All IA masses are restricted to motion in only the vertical direction. (b) Frequency band structure for the undamped and damped unit cells; results for the damped unit cells shown only for real wave numbers. (c) Damping-ratio diagrams for the damped unit cells. (d) Damping-emergence metric Z; for the AM, the summation of the two damping-ratio branches of the PnC has been used for the reference quantity (ζ_{sum}), and for the IAs, the average of the two damping-ratio branches of the PnC ($\zeta_{\text{sum}}/2$) has been used for the reference quantity as distinguished by the asterisk applied to the subscript 1. (e) Damping-emergence metric Z for the IA where damping ratio corresponding to the acoustic branch of the PnC is used for the reference quantity. In sub-figures (b) and (c), the subscripts '1', '2', and 'sum' indicate the acoustic branch, optical branch, and sum of the two branches, respectively.

$$\begin{bmatrix} m_1 & 0 \\ 0 & m_2 \end{bmatrix} \begin{Bmatrix} \ddot{u}_n \\ \ddot{w}_n \end{Bmatrix} + \begin{bmatrix} c + 2C(1-\cos\mu) & -c \\ -c & c \end{bmatrix} \begin{Bmatrix} \dot{u}_n \\ \dot{w}_n \end{Bmatrix} + \begin{bmatrix} k_{\text{AM}} + 2K_{\text{AM}}(1-\cos\mu) & -k_{\text{AM}} \\ -k_{\text{AM}} & k_{\text{AM}} \end{bmatrix} \begin{Bmatrix} u_n \\ w_n \end{Bmatrix} = \begin{Bmatrix} 0 \\ 0 \end{Bmatrix}. \tag{17}$$

We will first consider the IA chain with the local-resonator mass set as zero, i.e., $m = 0$. In this case, for the PnC and AM, we will assume $m_1 = M$ and $m_2 = m_a$. We will then consider a nonzero local-resonator mass and assume $m_1 = M + m_a$ and $m_2 = m$.

The dispersion relations of all models are computed from each corresponding Bloch-transformed system of equations for values of the propagation constant ranging from $\mu = 0 \rightarrow \pi$. The solution for the eigenvalue problem for a given μ is written as

$$\lambda_s(\mu) = -\zeta_s(\mu)\omega_{r_s}(\mu) \pm \mathrm{i}\omega_{d_s}(\mu), \tag{18}$$

where ω_{r_s} and ω_{d_s} are the resonant and damped wave frequencies, respectively, and ζ_s is the wavenumber-dependent damping ratio. The index $s = 1,2$ refers to the acoustic and optical dispersion branches, respectively.

Table 1
Parameters used for the unit-cell models examined in Figs. 1, 2, and 4.

Parameter	Fig. 1	Fig. 2	Units
M	1	1	Kg
m	-	0.1	Kg
m_a	0.1	0.1	Kg
K_{PnC}	120	120	Nm^{-1}
k_{PnC}	1320	1200	Nm^{-1}
K_{AM}	110	109	Nm^{-1}
k_{AM}	179	179	Nm^{-1}
K_{IA}	100	100	Nm^{-1}
k_{IA}	-	40	Nm^{-1}
$k_{\mathrm{IA}}{}^{*}$	-	500	Nm^{-1}
C	2	2	Nsm^{-1}
c	0	2	Nsm^{-1}

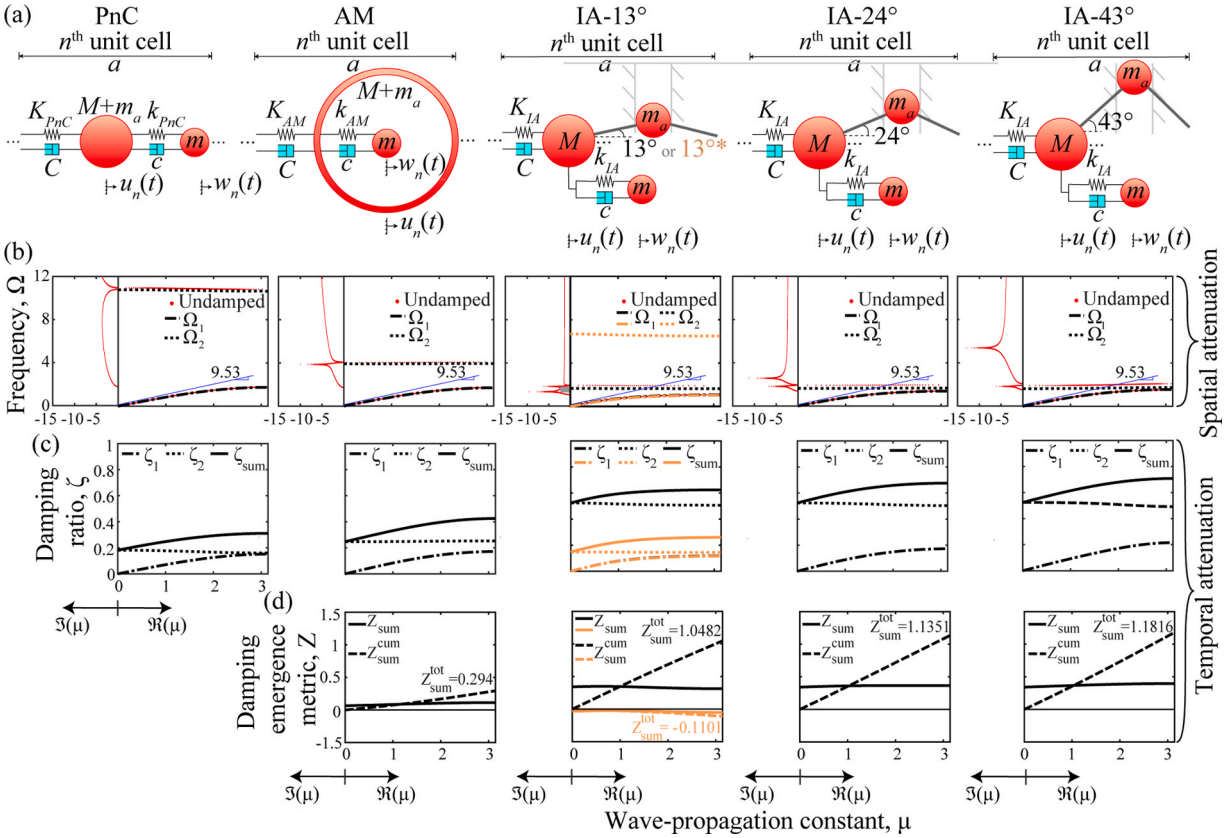

Fig. 2. Analysis of inertially amplified chain with a resonating mass. (a) Unit-cell schematics of statically equivalent chains, including a PnC, AM, and three variations of the IA chain exhibiting $\alpha = 13^{\circ}, 24^{\circ}$, and 43°, respectively. All IA masses are restricted to motion in only the vertical direction. (b) Frequency band structure for the undamped and damped unit cells; results for the damped unit cells only shown for real wave numbers. (c) Damping-ratio diagrams for the damped unit cells. (d) Damping-emergence metric Z. In sub-figures (a) and (b), the subscripts '1', '2', and 'sum' indicate the acoustic branch, optical branch, and sum of the two branches, respectively. The orange curves in the third column are the results for IA-13* which is statically equivalent to the PnC and obtained by only increasing the local-resonator stiffness of IA-13° from $k_{\mathrm{IA}} = 40\ \mathrm{Nm}^{-1}$ to $k_{\mathrm{IA}}{}^{*} = 500\ \mathrm{Nm}^{-1}$ for the purpose of illustrating negative metadamping at $\alpha = 13^{\circ}$.

3. Extreme levels of positive and negative metadamping

We first investigate an inertially amplified chain without a resonating mass, similar to an analysis done in Ref. [20]. The unit cell for this model is depicted in the third, fourth, and fifth panels in Fig. 1a for three different IA angles, $\alpha = 13^{\circ}, 24^{\circ}$, and 43°, respectively. These angles are arbitrarily chosen to represent qualitatively different behaviors. For comparison, a standard diatomic phononic crystal model and a mass-in-mass acoustic metamaterial model, each with the same long-wave speed of sound, $C_{\mathrm{stat}} = 0.99$, as the IA chain are considered. This provides us with five distinct chains that are all statically equivalent. The parameters used for all models are given in

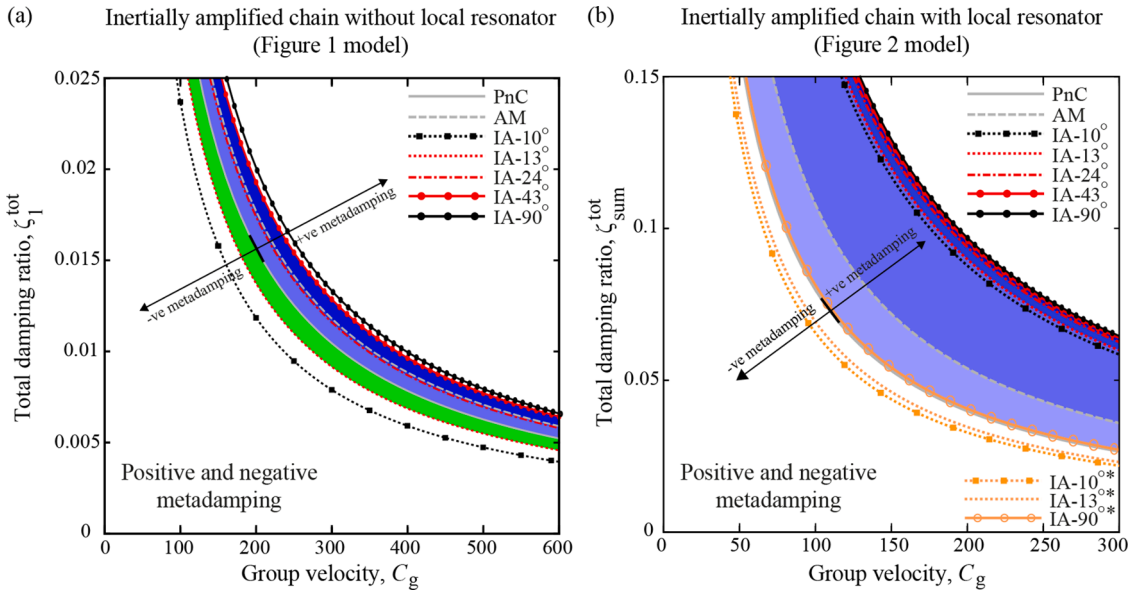

Fig. 3. Illustration of metadamping: total damping ratio based on the first branch ζ_1^{tot} or the sum of the two branches ζ_{sum}^{tot} versus long-wave speed of sound C_g in the periodic chains. (a) Positive or negative metadamping (depending on value of α) exhibited in the case of IA chain without a resonating mass; blue- and green-shaded areas represent regions of positive and negative metadamping, respectively. Maximum positive and negative metadamping are reached at IA-90° and IA-10°, respectively. (b) Positive metadamping exhibited in the case of inertially amplified chain with a resonating mass; blue-shaded area represents region of positive metadamping. Maximum positive metadamping is reached at IA-90°. The intensity of positive metadamping increases as the color of the blue shaded areas gets darker. The orange curves are the results for IA-10°*, IA-13°*, and IA-90°* which are also statically equivalent to the PnC and obtained by only increasing the local-resonator stiffness of the IA chain from $k_{IA} = 40\ \text{Nm}^{-1}$ to $k_{IA}{}^* = 500\ \text{Nm}^{-1}$ for the purpose of illustrating negative metadamping, which reaches its maximum at $\alpha = 10°$.

Table 1. The damped-frequency dispersion diagrams and corresponding damping-ratio diagrams for each of the five systems are given in Figs. 1b and 1c, respectively. In all frequency band-structure figures, we plot the dimensionless quantity $\Omega = \omega/\omega_b$, where $\omega_b = \sqrt{K_{PnC}/M}$ is defined as the base frequency. The complex dispersion curves for the undamped version of all models are also provided to show the frequency-dependent profile of spatial attenuation for each chain [26]. In Figs. 1d and 1e, the wavenumber-dependent damping-emergence metric Z, which is a measure of metadamping, is plotted; this metric is defined as [5]

$$Z_l(\mu)|_* = \zeta_l(\mu)|_* - \zeta_l(\mu)|_{PnC} \quad (l = 1,\ 2,\ \text{or sum}) \tag{19}$$

where the subscript "*" indicates AM or the IAs. It represents the difference between the damping ratio of the AM or each of the IA chains and that of the reference PnC case. The index l indicates the acoustic branch ($l = 1$), optical branch ($l = 2$), and the summation ($l = \text{sum}$) of the two branches. Any rise in $Z(\mu)$ above zero is indicative of positive metadamping, and, in contrast, a drop in $Z(\mu)$ below zero is indicative of negative metadamping. We also employ the cumulative and the total value of $Z(\mu)$ defined as

$$Z_l^{cum}(\mu) = \int_0^{\mu} Z_l\, d\mu \quad (\mu \in [0, \pi];\ l = 1,\ 2,\ \text{or sum}) \tag{20}$$

and

$$Z_l^{tot} = Z_l^{cum}(\pi) \quad (l = 1,\ 2,\ \text{or sum}) \tag{21}$$

respectively, to further quantify the difference in the damping ratio. The quantity Z_l^{cum} represents the integrated value of Z_l over the BZ, and upon complete integration over the BZ, the total value of Z_l, which is Z_l^{tot}, is calculated to give an overall quantification of the positive or negative damping capacity with respect to the reference PnC. Since the IA chain here has only one branch, the Z quantity indicated as Z_{1^*} in Fig. 1d is obtained by comparing the damping ratio of that branch with the average of the two damping-ratio branches, $\zeta_{sum}/2$, of the PnC. Alternatively, in Fig. 1e, the comparison is made with the damping ratio of the first branch of the PnC. It is observed from the results that for the parameters selected, as listed in Table 1, the IA chain exhibits positive metadamping with increasing levels as α increases and easily overcomes the levels attained by the AM.

We now attach a local resonator to the base of the IA chain as shown in the third, fourth, and fifth panel schematics of Fig. 2a. This

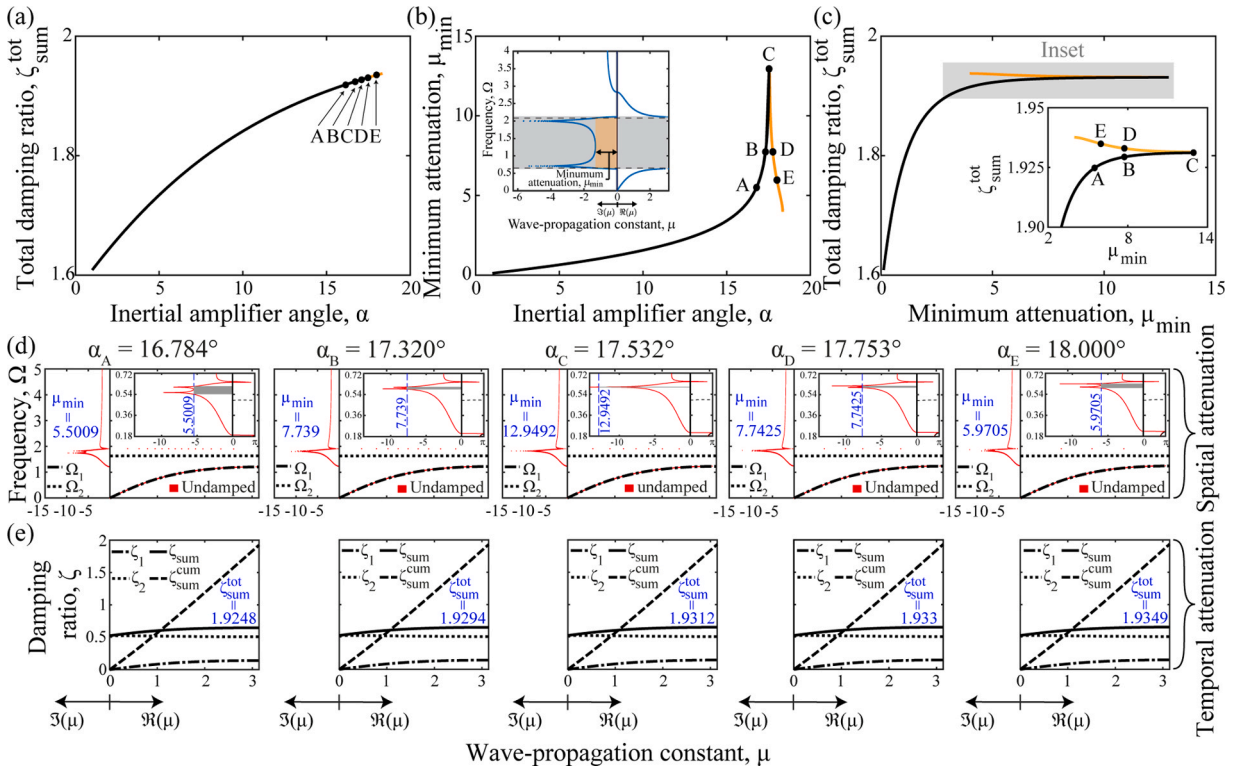

Fig. 4. Performance characteristics for the IA chain with a resonating mass. (a) Temporal-attenuation intensity: total damping ratio ζ_{sum}^{tot} versus inertial-amplifier angle α. (b) Spatial-attenuation intensity: minimum attenuation μ_{min} versus α; inset shows a schematic that defines the μ_{min} quantity. (c) Minimum attenuation μ_{min} versus total damping ratio ζ_{sum}^{tot}; inset in sub-figure (c) shows an enlarged version of the trade-off region. The points A-E, corresponding to five different values for α, have been specifically chosen and used to illustrate the evolution of the response with the angle α where a region is identified that features a trade-off between the temporal and spatial attenuation properties. (d) Frequency band structure corresponding to the five chosen values of α; insets show the corresponding plots with the y-axis reproduced in a log scale. Results for the damped IA chains are shown only for real wave numbers. (e) Damping-ratio diagrams corresponding to the five chosen values of α.

allows us to consider models with the same number of dispersion branches, and, importantly, generates an IA chain configuration that may exhibit a bounded band gap, as would an experimentally realizable material that is modeled as a continuum. An undamped version of this model has been recently investigated for spatial attenuation characteristics [26]. Here we observe a monotonic increase in positive metadamping, as expressed by the quantity Z_{sum}^{tot}, as we progress from an AM chain to an IA chain with increasing values of the lever-arm angle α. This demonstrates an extreme level of positive metadamping significantly exceeding what is realized by an AM. We consider a special case where we modify IA-13° to IA-13°* by only increasing the local-resonator stiffness from $k_{IA} = 40\ \mathrm{Nm}^{-1}$ to $k_{IA}{}^{*} = 500\ \mathrm{Nm}^{-1}$; by doing so, the IA chain, which remains statically equivalent to the PnC, shows a significant reduction in the total dissipation at $\alpha = 13°$ to the point where it starts to exhibit negative metadamping as evidenced by the orange curves in Fig. 2. By considering this special case, we have shown that the level of metadamping for a given lever-arm angle in an IA chain can be controlled, and altered significantly, by varying the value of the local-resonator stiffness while keeping the long-wave speed of sound unaltered. Fig. 3 extends the analysis of both models, the inertially amplified chain without (Fig. 3a) or with (Fig. 3b) a local resonator, to a broad range of quasi-static speeds extending well beyond the values considered in Figs. 1 and 2; this provides an Ashby-like map for the damping capacity versus the long-wave speed, which is representative of the effective quasi-static stiffness of the chain. The damping capacity is obtained by integrating the damping ratio over the BZ in the following manner:

$$\zeta_l^{cum}(\mu) = \int_0^{\mu} \zeta_l \, d\mu \quad (\mu \in [0, \pi];\ l = 1 \text{ or sum}) \tag{22}$$

and calculating its total value which is $\zeta_l^{tot} = \zeta_l^{cum}(\pi); l = 1$ or sum. Since the IA chains in Fig. 1 have only one damping-ratio branch, for a fair comparison, we only consider the first damping-ratio branch of the PnC and AM in Fig. 3a. We observe in Fig. 3a that the AM exhibits positive metadamping throughout the parameter range shown. We also observe that the inertially amplified chain (without a

resonator) exhibits even more positive metadamping for $\alpha = 43^{\circ}$; however, the level of metadamping decreases as α decreases. Eventually, for $\alpha = 13^{\circ}$, the metadamping is shown to be strongly negative, i.e., the IA chain exhibits less loss overall compared to the statically equivalent PnC. A maximum value of negative metadamping is reached at $\alpha = 10^{\circ}$; at lower angles the static equivalence is no longer maintained. In Fig. 3b, where a separate local resonator is attached to the IA chain, we observe positive metadamping with increasing intensity as the lever-arm angle α increases. In both Fig. 3a and Fig. 3b, we also show the performance for the IA chain at $\alpha = 90^{\circ}$; such an angle is practically unrealizable, but it gives the maximum theoretical limit for the metadamping level shown by each IA chain. The special case IA-13* considered in Fig. 2 is also extended and shown in Fig. 3b, along with two corresponding special cases, for IA-10° and IA-90° (similarly represented by IA-10* and IA-90*). Consistent with the results of Fig. 2, we observe a significant decrease in metadamping with IA-13* exhibiting negative metadamping, and IA-10* exhibiting maximum negative metadamping.

4. Regime displaying trade-off between temporal attenuation and spatial attenuation

In Fig. 4, we expand our examination of the IA chain with a local resonator (using the same parameters listed in Table 1) and further examine the effects of the lever-arm angle α on the total damping ratio; i.e., on the intensity of the temporal attenuation, which is a measure of total dissipation. However, we also examine its effect on the imaginary-wavenumber part of the spectrum, which represents the spatial attenuation. As shown in [26], for a certain range of α, the attenuation peak associated with the IA mechanism couples with the attenuation peak associated with the local resonator. This yields a coupled double-attenuation peak, within a bounded band gap, in the imaginary-wavenumber part of the dispersion diagram. We can quantify the strength of this attenuation by evaluating the minimum value of imaginary wave propagation constant bounded by the two peaks; we denote this quantity by $\mu_{\min}$ (see inset of Fig. 4b [26]).

Using $\zeta_{\text{sum}}^{\text{tot}}$ and $\mu_{\min}$, Figs. 4a and 4b, respectively, show the variation of the temporal- and spatial- attenuation intensities with the IA lever-arm angle α. Fig. 4c combines these two relations in one plot, showing the temporal attenuation versus the spatial attenuation. It is observed that the two measures increase monotonically up to a specific angle, $\alpha = 17.532^{\circ}$. However, as the angle increases further, a trade-off is observed between the intensity of temporal attenuation and the intensity of spatial attenuation. To the best of the authors' knowledge, this represents an unprecedented space-time attenuation trade-off phenomenon for an elastodynamic medium. This trade-off is observed until $\alpha = 18.348^{\circ}$ beyond which the coupled double-peak feature in the spatial-attenuation spectrum no longer exists; hence, the $\mu_{\min}$ measure is no longer valid. Figs. 4d and 4e show, respectively, the frequency and damping-ratio diagrams for a selection of points in the parameter space, as marked in Fig. 4c.

5. Conclusions

We have demonstrated that inertial amplification provides a route to yielding a structured material with simultaneously high stiffness and high damping capacity (positive metadamping) or low stiffness and low loss (negative metadamping). The levels of positive or negative metadamping attained are elevated and well exceed the performance of conventional elastic metamaterials. These attributes extend the boundaries of viscoelastic dynamical properties of state-of-the-art structured-material systems. Furthermore, when combining the inertial amplification with local resonance, we observe the unique phenomenon of a trade-off between the temporal- and spatial-attenuation intensities in the material properties for a given range of IA angle α. This is realized passively and by only changing the lever-arm angle in the IA chain. By appropriate adjustment of this angle, another regime is also realized that exhibits monotonic increase in both attenuation types. These traits open the way for the design of future phononic materials with tailored space-time attenuation characteristics and could have significant implications on topological phononics and other contemporary areas in phonon engineering.

Declaration of Competing Interest

The authors declare that they have no known competing financial interests or personal relationships that could have appeared to influence the work reported in this paper.

Appendix

The dispersion and attenuation characteristics of the IA metamaterial chain is intricately dependent on the unit cell's various design parameters. Using Fig. A1, we introduce certain non-dimensional parameters associated with an IA unit cell. The parameter $\theta = m_a/M$ is the ratio of the IA mass to the baseline mass and $\beta = \theta/4\tan^2\alpha = m_a/4M\tan^2\alpha$ represents this same ratio with consideration of the influence of the IA angle α. Thus, the parameter β directly represents the level of the effective inertial amplification by the IA mass due to a variation of the IA angle α. It can be seen that the value of β drastically increases as α decreases and nearly linearly increases with θ. Note that in the unamplified static state, the effective value of this mass is equal to its given value of m_a. The factor $4\tan^2\alpha$ in the definition of β indicates the level of inertial amplification; the higher this level is, the higher the effective value of m_a and the stronger the impact on the dispersion and attenuation characteristics.

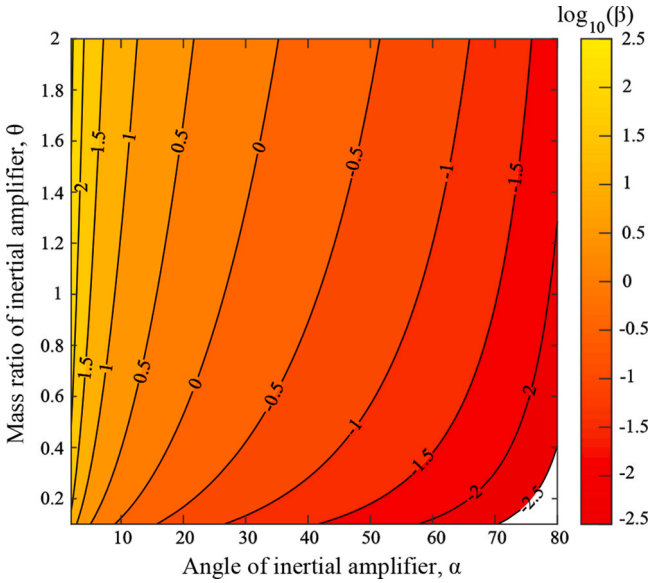

Fig. A1. Non-dimensional parameter β as a function of inertial-amplifier mass ratio (ratio of inertial-amplifier mass to baseline mass) θ and the inertial-amplifier angle α.

References

[1] S. Mukherjee, E.H. Lee, Dispersion relations and mode shapes for waves in laminated viscoelastic composites by finite difference methods, Comput. Struct. 5 (1975) 279.
[2] M.I. Hussein, Theory of damped Bloch waves in elastic media, Phys. Rev. B 80 (2009), 212301.
[3] M.I. Hussein, M.J. Frazier, Band structure of phononic crystals with general damping, J. Appl. Phys. 108 (2010), 093506.
[4] M.I. Hussein, M.J. Frazier, M.H. Abedinnasab, Chapter 1: Microdynamics of phononic materials, in: S. Li, X.-L. Gao (Eds.), Handbook of Micromechanics and Nanomechanics, Pan Stanford Publishing, 2013, pp. 1–28.
[5] M.I. Hussein, M.J. Frazier, Metadamping: An emergent phenomenon in dissipative metamaterials, J. Sound Vib. 332 (2013) 4767.
[6] P.A. Deymier, Acoustic Metamaterials and Phononic Crystals, Springer, 2013.
[7] M.I. Hussein, M.J. Leamy, M. Ruzzene, Dynamics of phononic materials and structures: Historical origins, recent progress, and future outlook, Appl. Mech. Rev. 66 (2014).
[8] A.S. Phani, M.I. Hussein, Dynamics of Lattice Materials, John Wiley & Sons, 2017.
[9] M.M. Sigalas, E.N. Economou, Elastic and acoustic wave band structure, J. Sound Vib. 158 (1992) 377.
[10] M.S. Kushwaha, P. Halevi, L. Dobrzynski, B. Djafari-Rouhani, Acoustic band structure of periodic elastic composites, Phys. Rev. Lett. 71 (1993) 2022.
[11] V. Laude, Phononic Crystals: Artificial Crystals for Sonic, Acoustic, and Elastic Waves, de Gruyter Co, Berlin, Germany, 2015.
[12] Z. Liu, X. Zhang, Y. Mao, Y.Y. Zhu, Z. Yang, C.T. Chan, P. Sheng, Locally resonant sonic materials, Science 289 (2000) 1734.
[13] Y. Jin, Y. Pennec, B. Bonello, H. Honarvar, L. Dobrzynski, B. Djafari-Rouhani, M. Hussein, Physics of surface vibrational resonances: pillared phononic crystals, metamaterials, and metasurfaces, Rep. Prog. Phys. 84 (2021), 086502.
[14] C.L. Bacquet, H. Al Ba'ba'a, F.M. J, M. Nouh, M.I. Hussein, Metadamping: Dissipation emergence in elastic metamaterials, Advances in Applied Mechanics 51 (2018) 115.
[15] M.J. Frazier, M.I. Hussein, Viscous-to-viscoelastic transition in phononic crystal and metamaterial band structures, J. Acoust. Soc. Am. 138 (2015) 3169.
[16] C.L. Bacquet, M.I. Hussein, Dissipation engineering in metamaterials by localized structural dynamics, arXiv:1809.04509 (2018).
[17] D. DePauw, H. AlBa'ba'a, M. Nouh, Metadamping and energy dissipation enhancement via hybrid phononic resonators, Extreme Mechanics Letters 18 (2018) 36–44.
[18] A. Aladwani, M. Nouh, Mechanics of metadamping in flexural dissipative metamaterials: Analysis and design in frequency and time domains, Int. J. Mech. Sci. 173 (2020), 105459.
[19] I. Antoniadis, D. Chronopoulos, V. Spitas, D. Koulocheris, Hyper-damping properties of a stiff and stable linear oscillator with a negative stiffness element, J. Sound Vib. 346 (2015) 37–52. –.
[20] H. Al Ba'ba'a, Z. Lin, S. Tol, Metadamping enhancement and tunability via scissor-like electromechanical metamaterials, J. Appl. Phys. 130 (2021), 184901.
[21] J. Callanan, C. Willey, V. Chen, J.J. Liu, M. Nouh, A. Juhl, Uncovering low frequency band gaps in electrically resonant metamaterials through tuned dissipation and negative impedance conversion, Smart Mater. Struct. 31 (2021), 015002.
[22] C. Yilmaz, G.M. Hulbert, N. Kikuchi, Phononic band gaps induced by inertial amplification in periodic media, Phys. Rev. B 76 (2007) 54309.
[23] C. Yilmaz, G.M. Hulbert, Theory of phononic gaps induced by inertial amplification in finite structures, Phys. Lett. A 374 (2010) 3576.
[24] G. Acar, C. Yilmaz, Experimental and numerical evidence for the existence of wide and deep phononic gaps induced by inertial amplification in two-dimensional solid structures, J. Sound Vib. 332 (2013) 6389.
[25] N.M.M. Frandsen, O.R. Bilal, J.S. Jensen, M.I. Hussein, Inertial amplification of continuous structures: Large band gaps from small masses, J. Appl. Phys. 119 (2016), 124902.
[26] A. Banerjee, S. Adhikari, M.I. Hussein, Inertial amplification band-gap generation by coupling a levered mass with a locally resonant mass, Int. J. Mech. Sci. 207 (2021), 106630.